═══REVIEW COMMONS MANUSCRIPT═══

IMPORTANT:

- Manuscripts submitted to Review Commons are peer reviewed in a journal-agnostic way.
- Upon transfer of the peer reviewed preprint to a journal, the referee reports will be available in full to the handling editor.
- The identity of the referees will NOT be communicated to the authors unless the reviewers choose to sign their report.
- The identity of the referee will be confidentially disclosed to any affiliate journals to which the manuscript is transferred.

GUIDELINES:

- For reviewers: https://www.reviewcommons.org/reviewers
- For authors: https://www.reviewcommons.org/authors

CONTACT:

The Review Commons office can be contacted directly at: office@reviewcommons.org

Title

Tunneling Nanotube–like Connections in the Developing Cerebellum: Distinct from Cytokinetic and Intercellular Bridges

Authors

Malalaniaina Rakotobe[1,2*], Garima Virmani[1], Shiyu Liu[1], Gabriel Kaddour[3], Nathaly Dongo Mendoza[1], Jean Livet[3], Laurence Cathala[2], Chiara Zurzolo[1*]

Affiliation

[1]Membrane Traffic and Pathogenesis, Institut Pasteur, Université Paris Cité, CNRS UMR 3691, F-75015 Paris, France.
[2]Sorbonne Université, Institut du Cerveau - Paris Brain Institute - ICM, Inserm, CNRS, APHP, Hôpital de la Pitié Salpêtrière, Paris, France
[3]Sorbonne Université, INSERM, CNRS, Institut de la Vision, Paris 75012, France
Corresponding authors: chiara.zurzolo@pasteur.fr (Chiara Zurzolo), malalaniainarakotobe@gmail.com (Malalaniaina Rakotobe)

Abstract

Intercellular communication is essential for brain development. While classical communication modes—such as paracrine, juxtacrine and synaptic signaling—are well characterized, emerging evidence suggests that tunneling nanotubes (TNTs), membranous bridges primarily observed *in vitro,* may also contribute. However, their presence and function *in vivo* remain unclear, partly due to the challenge of distinguishing them from other types of intercellular connections (ICs). Building on prior evidence of ICs in the external granule layer (EGL) of the developing cerebellum, we investigated their nature in postnatal day 7 (P7) mice. Using immunofluorescence and genetically sparse labeling, we distinguished cytokinetic bridges (CBs), transient connections formed between daughter cells during the final stage of cell division, and intercellular bridges (IBs), more stable connections that persist after division, from TNT-like structures, which form independently of cell division. We observed CBs but not IBs in the EGL. We also observed TNT-like connections throughout the EGL, which appeared to

[1] The present address of M.R is at NBX Biosciences, 34000 Montpellier, France; G.V is at Instytut Biologii Doświadczalnej im. M. Nenckiego PAN, 02-093 Warszawa, Poland; N.D.M is at The EKFZ for *Digital* Health, 01307 Dresden, Germany; L.C is at University of Colorado Anschutz Medical Campus, 80045 CO, USA

connect both clonally and non-clonally related cells. The presence of these TNT-like structures in the developing EGL suggests that TNT-like connections may contribute to intercellular communication, paving the way for further study of a previously unrecognized mechanism that could influence neuronal fate, migration, and network formation during cerebellar development.

Keywords

Intercellular communication, intercellular connections (ICs), tunneling nanotubes (TNTs), cytokinetic bridges (CBs), intercellular bridges (IBs), cerebellum development.

Introduction

Intercellular communication plays a crucial role in brain development, ensuring the precise regulation and coordination of processes including neurogenesis, cell migration, differentiation and the establishment of functional neuronal networks. This communication occurs through the secretion of extracellular vesicles and soluble molecules (Bahram Sangani et al., 2021; Sahay et al., 2020), as well as through synaptic interactions via electrical and chemical synapses (Pereda, 2014). Disruptions in these pathways can lead to neurodevelopmental disorders, highlighting their significance in brain maturation.

Beyond classical mechanisms, recent studies have identified additional structures involved in intercellular communication, including cytonemes, intercellular bridges (IBs), and tunneling nanotubes (TNT) (Korenkova et al., 2020). Cytonemes are thin, F-actin-based, close-ended protrusions (1–700 µm in length) that mediate signal transduction between cells via membrane-tethered receptors and ligands, without establishing cytoplasmic continuity (Hall et al., 2024). IBs (0.4–350 µm in length) arise from incomplete cytokinesis and allow cytoplasmic exchange between connected cells (Haglund et al., 2011; Rujano et al., 2022). Unlike cytokinetic bridges (CBs), which are abscised at the end of cytokinesis, IBs persist longer, facilitating sustained communication between connected cells. TNTs, which can extend up to 200 µm, are F-actin based, open-ended membranous structures, formed *de novo* between two distinct cells. They facilitate the transfer of cargo such as organelles, proteins, and nucleic acid. The open-ended nature of TNTs can be assessed using high-resolution electron microscopy (EM) or live imaging which demonstrates uninterrupted transfer of large cargo such as organelles (Sáenz-de-Santa-

María et al., 2023). However, these techniques are difficult to apply to tissue samples. Identifying TNTs in *vivo* is particularly challenging due to the lack of specific molecular markers, the fragility of these structures, and their sensitivity to fixative like paraformaldehyde, which can compromise structural preservation. Consequently, such structures are typically referred to as "TNT-like" in tissue until their ability to transfer cellular cargos between connected cells is confirmed (Palese et al., 2025). Due to these hurdles, TNTs have been extensively studied *in vitro*, but their *in vivo* characterization remains limited, with only recent evidence confirming functional TNTs in the zebrafish embryo (Korenkova et al., 2024).

In the developing cerebellum, the external granule layer (EGL) constitutes a dynamic region where granule cells (GCs), the most numerous neurons of the brain, are generated. Granule cell progenitors (GCPs) proliferate in the outer EGL (oEGL) for approximately three weeks before differentiating into postmitotic GCs which migrate through the inner EGL (iEGL) and molecular layer to reach the inner granular layer (IGL) (Consalez et al., 2020). Intercellular communication within the EGL is essential for coordinating interactions not only between GCs but also with other neuronal populations (Kim et al., 2023). Combining serial-section electron microscopy (ssSEM) with computational connectomics in fixed tissue, we have recently identified intercellular connections (ICs) linking immature GCs in the mouse EGL. By analyzing cellular parameters such as shape, Golgi apparatus number, and cilium presence, our data suggested that these structures could represent either stable IBs or TNTs. However, their precise nature and function could not be precisely determined since this approach does not allow the use of specific markers to distinguish IBs from other types of cellular connections (Cordero Cervantes et al., 2023).

In this study, we investigated the presence and characteristics of IBs and TNT-like connections in the EGL of postnatal day 7 (P7) mice. Using immunofluorescence and genetic labeling techniques, we distinguished CBs and IBs from TNT-like connections. While CBs were identified in the iEGL, our findings indicate that these do not account for all previously observed ICs (Cordero Cervantes et al., 2023), supporting the existence of TNT-like connections that may facilitate intercellular communication. Although further investigation is needed to determine the functional role of these structures, our results highlight a previously unrecognized mode of cellular interaction during cerebellar development, with potential implications for neuronal migration and network formation.

Material and methods

Animals

All mice used were generated and maintained in the animal facility of the Institut Pasteur, Paris. The care and handling of the animals prior or during the experimental procedures followed European Union rules and were approved by the French Animal Protection Committee and the local Ethics Committees. Animals were maintained on a 12h light/dark cycles with food and water provided ad libitum. C57BL/6 mice at P7 were used for the quantification of CBs and mitotic cells in the iEGL. Rj:SWISS mice were used for the electroporation of the *pCAG-Dendra2-E2A-EGFP-Cep55* plasmid.

Transgenic mouse lines

CAG-Cytbow reporter line was generated using a pronuclear injection strategy to insert the *Cytbow* MAGIC Marker transgene into C57BL6/J genetic background (Loulier et al., 2014). This reporter enables stochastic expression of mTurquoise2, mEYFP and tdTomato under the control of the ubiquitous CAG promoter in a Cre-dependent manner (this line will be described elsewhere). To generate experimental animals, we crossed homozygous *CAG-Cytbow*$^{+/+}$ males with *Nestin-CreER*$^{T2+/-}$ females (Lagace et al., 2007) to obtain *Nestin-CreER*$^{T2+/-}$*; CAG-Cytbow*$^{+/-}$ offspring. To increase the probability of combinatorial fluorescent protein expression of in a Cre-dependent manner, these *Nestin-CreER*$^{T2+/-}$*; CAG-Cytbow*$^{+/-}$ females were backcrossed with *CAG-Cytbow*$^{+/+}$ males to generate *Nestin-CreER*$^{T2+/-}$*; CAG-Cytbow*$^{+/+}$experimental animals.

Tamoxifen injection

To sparsely label neural cells, *Nestin-CreER*$^{T2+/-}$*; CAG-Cytbow*$^{+/+}$ newborns received subcutaneous injection of 25µL of tamoxifen (234-118-0, Merck) diluted in corn oil once per day at P0, P1, P2 and P3 at a concentration of 5 mg/mL.

Plasmid

Coding sequence of *pCAG-Dendra2-E2A-EGFP-Cep55* construct was cloned from *pDEST-Dendra2-E2A-EGFP-Cep55* construct (used in Korenkova et al., 2024) into the *pCAG-GFP* plasmid from Addgene (Plasmid #11150).

Postnatal electroporation

Vetergesic, at a concentration of 0.05 mg/kg, was injected 30 minutes prior to surgery for analgesia. Anesthesia was induced with 4% isoflurane for 10 minutes and then maintained at 2% throughout the procedure. Before making the incision, laocaine at a concentration of 2.5 mg/kg was injected at the incision site to alleviate pain. To prevent desiccation, the eyes were protected with Ocry-gel. Following the craniotomy, the *pCAG-Dendra2-E2A-EGFP-Cep55* plasmid was injected at the surface of the cerebellum using a glass micropipette. The plasmid was delivered at 4–5 sites for a total injection volume of 1 µl at a concentration of 5.9 µg/µl. Triple electrodes coated with conductive gel were used for electroporation. The electrode connected to the anode was placed on a micromanipulator and lowered into contact with the craniotomy under optical control, while the two cathode electrodes were positioned on either side of the animal's head. Electroporation (using a BTX electroporator) was performed immediately, with the following parameters: 5 pulses of 50 ms at 1 Hz, at 80V. Immediately after electroporation, the mouse was placed on a heating pad and stimulated to restart respiration in case of cardiorespiratory arrest. The incision was sealed with Vetbond surgical glue, and a subcutaneous injection of 20-30 µl of 0.9% NaCl was administered gently to hydrate the mouse.

Live imaging of acute cerebellar slices

This protocol was adapted from a Star Protocol by Qu. X et al. (Qu et al., 2021). Briefly, pups were decapitated and the brain dissected in oxygenated, ice-cold complete HBSS (cHBSS) buffer. The brain was then transferred to the slicing chamber of a vibratome (Leica Biosystem VT 1000S), which contained cHBSS to keep the brain submerged, while oxygenation is maintained in the chamber. Brain slices (250 µm thick) were prepared using the vibratome at a speed of 0.08–0.1 mm/s and collected in a "nest beaker" containing complete cHBSS medium, bubbled at 33°C. Cerebellar slices expressing fluorescent reporters were selected and transferred to a µ-Slide 8 Well (ibidi, Cat. No: 80807) with 1 mL of warm, fresh, sterile medium. The ibidi well were placed in a temperature-controlled chamber attached to the microscope,

where both temperature (37°C) and CO_2 flow (5%) were regulated and maintained to promote cell viability and ensure optical stability during live imaging.

Component of the complete HBSS	Stock concentration	Final concentration	Volume
HBSS (Thermo Fisher, 14065056)	10x	1x	50 mL
HEPES (pH 7.4) (Thermo Fisher, 15630080)	1 M	2.5 mM	1.25 mL
D-Glucose (Sigma-Aldrich, G8270)	1 M	30 mM	15 mL
CaCl2 (Sigma-Aldrich, C5670)	100 mM	1 mM	5 mL
MgSO4 (Sigma-Aldrich, M2643)	100mM	1mM	5 mL
NaHCO3 (Sigma-Aldrich, 144-55-8)	1 M	4 mM	2 mL
ddH2O			421.75 mL
Total			500 mL
Sterile filter with a 0.2 µm filter. Store at 4°C.			

Immunohistochemistry

Brains were dissected and fixed overnight in 4% paraformaldehyde (PFA) at 4°C, then rinsed in PBS and cryoprotected in 30% sucrose in PBS at 4°C overnight before embedding and freezing in OCT (Cryomatrix™, Thermo) at −80°C. The cerebellum was sliced in sagittal sections of 40 µm using a Leica CM 3050S cryostat. Sections were then mounted on SuperFrost+ slides (Fisher Scientific). Slices underwent an antigen unmasking step: they were incubated in unmasking solution (citrate buffer, pH 6) for 15 minutes in the 2100 Antigen Retriever. They were then cooled in PBS for 10 minutes before being permeabilized for 10 minutes in PBS containing 0.5% Triton. Next, slices were incubated for 1 hour in blocking solution (PBS with 5% fetal calf serum (FCS) and 2% bovine serum albumin (BSA)). To quantify CBs and mitotic cells, two rabbit-derived primary antibodies were used sequentially (the rabbit anti-Aurora B kinase antibody and the rabbit anti-Ki67 antibody). For those samples a two-step IHC was run. First, slices were immuno-labelled with the rabbit anti-Aurora B primary antibody before running a second IHC with the other antibodies including the rabbit anti-Ki67 antibody. The first Rabbit antibody was included in the blocking solution at room temperature for 2 hours. After PBS washes, the slices were incubated overnight at 4°C with a Fab fragment secondary antibody in blocking solution. Then the second step of the IHC

procedure was the same for all samples. Primary antibodies were incubated overnight at 4°C in blocking solution. The next day, secondary antibodies were incubated for 2 hours at room temperature in blocking solution. Finally, sections were incubated with DAPI (1 µg/ml) in PBS for 30 minutes and mounted using Fluoromount-Gold. Primary antibodies used were: rabbit anti-Aurora B kinase (Abcam, ab2254, 1:500), rabbit anti-Ki67 (Abcam, ab15580, 1:200), goat anti-TAG1 (rndsystems, AF4439, 1:200), mouse anti-citron kinase (BD Biosciences, 611376, 1:200), goat anti-anillin (Abcam, ab5910, 1:50), rabbit anti-anillin (Bethyl laborories, A301-406A, 1:500), chicken anti-GFP (Aves Lab, GFP-1010, 1:1000), goat anti-tdTomato (Sicgen, AB8181, 1:200), rat anti-PH3 (Abcam, ab10543, 1:200).

Secondary antibodies used (Jackson ImmunoResearch, 1:500) were: Fab Fragment anti-rabbit Alexa Fluor™647, anti-rabbit Alexa Fluor™594, anti-rabbit Alexa Fluor™647, anti-goat Alexa Fluor™488, anti-mouse Alexa Fluor™488, anti-goat Alexa Fluor™647, anti-chicken 488, anti-goat Alexa Fluor™594, anti-rat Alexa Fluor™488.

Microscopy and image analysis

Imaging

Images of brain sections were acquired on a zeiss LSM900 confocal microscope, except for a subset of samples electroporated with the *pCAG-Dendra2-E2A-EGFP-Cep55* plasmid which were imaged on a Nikon Ti2E Spinning disk microscope. In addition, a Leica SP8 confocal microscope was used to image the 4 fluorescent proteins (eBFP2, mTurquoise2, mEYFP, tdTomato) in the *Nestin-CreERT2+/-; Cytbow+/+* line.

The Zeiss LSM900 was equipped with a 63x/1.4 NA oil-immersion objective (**Fig. 1, 2, 4, S3E**) and a 10x/0.45 NA DRY objective (**Fig. 3B, S2 and S4D**), as indicated on the figure legends. Images were acquired at 16-bit depth, with a pixel size of 0,0706 µm and a z-step size of 0,35µm. The following fluorochromes and detection settings were used: DAPI (excited at 405 nm, emission detected at 415-480 nm), Alexa Fluor 488 (488 nm, 500-550 nm), Alexa Fluor 594 (561 nm, 580-620 nm), and Alexa Fluor 647 (633 nm, 640-700 nm).

The Nikon Ti2E inverted microscope was equipped with a Yokogawa CSU-W1 spinning disk unit and a Photometrics Prime 95B back-illuminated sCMOS camera. A 60x/1.4 NA oil-

immersion objective was used (**Fig. 3C, 3F**). Images were collected in 12-bit mode, with a pixel size of 0,108 µm and a z-step of 0,3 µm. Standard bandpass filters optimized for each fluorophore were used including 447/60 for DAPI and 525/50 for AF488.

The Leica SP8 confocal microscope was used with either a 20x/0.75 NA water immersion objective (**Fig. S3B**) or a 63x/1.4 oil-immersion oil objective (**Fig. S3C**), as indicated in the figure legends. Images were collected in an 8-bit mode for low-magnification tile scans (**Fig. S3B**) and in 16-bit mode for high resolution acquisition (**Fig. S3C**). For the 20x objective, the pixel size was 1,1359 µm with a z-step of 3,8 µm. For the 63x objective, images were single tiles with a pixel size of 0,0901 µm and a z-step of 0,2985 µm. A 405 nm laser and white laser (470-670) were used to excite the following fluorophores: eBFP2 (excited at 405 nm, emission detected at 415-465 nm), mTurquoise2 (excited at 470 nm, emission detected at 480-530 nm), mEYP (excited at 514 nm, emission detected at 524-574 nm), tdTomato (excited at 554 nm, emission detected at 564-604 nm).

Quantification of mitotic cells and CBs in the iEGL

For the quantification of CBs and mitotic cells in the iEGL, counts were normalized to the total number of nuclei in the iEGL. Nuclei were segmented using a muti-step computational pipeline. First, a convolutional neural network (U-Net) deep learning model was used to segment nuclei across confocal image stacks (**Fig. S1A**). The resulting segmentation masks were then used to remove background signals from pre-processed images.

Next, nuclear detection and quantification were performed in 2D using Cellpose, an anatomical segmentation algorithm (Stringer et al., 2021). Cellpose counted nuclei in individual z-slices, and this approach proved to be more reliable than the previously used watershed algorithm (**Table 1**). To estimate the number of nuclei in 3D, we derived a correction factor ($\bar{F}$) to scale Cellpose-based 2D counts to reflect the full z-stack volume. This factor was obtained by comparing automatic Cellpose 2D count from representative single slices to manual 3D annotations across the entire z- stack. The correction factor Fi for each region was calculated as below and applied uniformly to all images:

$$Fi = \frac{Manual\ 3D\ count}{Cellpose\ 2D\ count} \quad \text{.... (Eq 1)}$$

Sample	Region	Cellpose 2D count	Manually count		Relative error (%)	Correction Factor (Fi) (according to Eq. 1)
			2D	3D		
Sample 1	Region n°1	547	503	56	8.75%	0.11
Sample 2	Region n°2	735	692	62	6.21%	0.09
Sample 3	Region n°3	695	668	62	4.04%	0.09
				Average	6.33 %	0.092

Table 1. Estimation of a 2D-to-3D correction factor for Cellpose-based nucleus counting. *Correction factors were derived by comparing Cellpose 2D counts to manual annotations of the same slice (Manual 2D count) and to the full Z-stack (Manual 3D Count). Relative Error quantifies the discrepancy between Cellpose 2D and manual 2D counts. The average Correction Factor (F_i)=0,092 was then used to extrapolate total 3D counts from Cellpose 2D count across the full dataset.*

Nuclei segmentation

Nuclei segmentation was executed with a U-Net CNN (VGG-16 encoder) in four sequential steps: data preparation, learning, testing, and inference. During data preparation, 3-D multi-channel TIFF volumes were imported and channel 4 (DAPI) was selected as the sole input for segmentation; each slice was linearly rescaled to 0-255 and its brightness and contrast automatically equalised. Binary ground-truth masks of individual nuclei were generated manually in VAST (Berger et al., 2018).

For training, each 3D image volume was divided into overlapping tiles of size 1x320x320 pixels (Z, X, Y), with a stride of 1x270x270 pixels. Pixel dimensions were calibrated to 0.35 µm/pixel in X and Y axes, and the Z-spacing between slices was 3.5 µm. All image tiles were rescaled before training and split randomly into training (80%) and test (20%) sets.

To minimize overfitting, the training pipeline applied on-the-fly geometric and intensity augmentations, including random rotations, horizontal and vertical flips, ±10% translations, and ±20% contrast adjustments. During inference, only resizing to (320, 320) pixels was performed to match the input size expected by the network. The U-Net model was trained for 40 epochs

using the Adam optimizer (initial learning rate: 1×10^{-4}) with a batch size of 2. A sigmoid activation function was used for binary segmentation. Model selection was based on the best intersection-over-union (IoU) score achieved on the validation set.

During inference, the trained model was applied to the full 3D volumes using a sliding-window approach with the same tile size and overlap used during training. For each tile, probability maps were generated and subsequently thresholded at 0.5 to produce binary masks. These masks were then stitched together to reconstruct the entire segmented volume. Post-processing steps included filling internal holes and removing border-touching objects to refine the final segmentation. The resulting masks were used to isolate nuclei and eliminate background signals, enabling accurate quantification.

EGL and iEGL classification

The classification of the iEGL followed the same steps as the segmentation model. (**Fig. S1B**). During pre-processing, two additional immunofluorescence channels were incorporated alongside channel 4 (DAPI): channel 2 (Miller et al.) and channel 3 (Hanzel et al.). Each channel (Ki67, TAG1, and DAPI) was independently adjusted for brightness and contrast and subsequently merged to generate multi-channel composite inputs for classification. Volumes were split into non-overlapping patches of 100×100 pixels (X, Y) with a step size of 100 pixels. According to metadata extracted from the original TIFF files, the pixel size was calibrated to 0.35 µm per pixel, meaning that each patch corresponded to an area of approximately 35µmx35 µm in X-Y. The CNN architecture was the same as described in our previous paper (Cordero Cervantes et al., 2023). The network architecture consisted in three convolutional blocks with increasing filter sizes (16, 32, 64), each followed by max-pooling, and a final dense layer of 128 units before the classification output. A dropout layer (rate 0.2) was applied prior to the dense layers to reduce overfitting. Input images were resized to 100x100 pixels, and pixel values were normalized to the [0, 1] range. The training dataset consisted of randomly chosen and manually labeled iEGL and Background tiles. A total of 5488 random tiles were used for training and 1372 for validation. To enhance model generalization, data augmentation was applied during training, including random horizontal flips, ±10% rotations, and ±10% zoom.

For iEGL class after filtering: 2658 tiles (Training: 2126, Test: 532)

For Background class after filtering: 8404 tiles (Training: 6723, Test: 1681)

The model that provided the smallest loss was selected. The final model achieved F1-scores of 0.99897541 for iEGL and 0.99833055 for background on the test data. For inference on full image volumes, the pre-processed volumes were divided into patches of 100×100 pixels. The classification using CNN was then applied, and all patches with a probability greater than 0.5 of being iEGL and a probability less than 0.6 of being background were classified as iEGL.The resulting classified patches were reconstructed into binary masks delineating the iEGL. To generate the full EGL mask, the post-processed iEGL mask was expanded by padding, with the padding direction (left, right, up, down, right-up, or left-down) manually selected depending on the anatomical orientation of the EGL in the ima (Fig. S1C). (**Fig. S1C**).

The number of nuclei in the iEGL was determined by segmenting nuclei in 2D and counting those that overlapped with the iEGL mask. To estimate the corresponding 3D nuclear count, the 2D count was multiplied by the previously derived scaling factor $\bar{F}$=0.092 (**Fig. S1D**). The same approach was used to quantify the nuclei in the EGL (**Fig. S1D'**).

Image analysis

2D images were processed with Fiji (ImageJ). 3D renderings of acquired z-stacks were generated using Imaris® software (version 10, Oxford Instruments) to identify TNT-like connections. These structures were identified based on morphological criteria: a membranous protrusion was counted as a TNT-like connection if it appeared continuous, did not express CBs or IBs markers, and connected two labelled cells. The total number of labelled cells was counted manually using the Spots function in Imaris. The length of every TNT-like connection was measured using the Measurement points tool.

Quantification and statistical analysis

Statistical analysis was performed using Microsoft Excel and GraphPad Prism. To compare relative numbers of CBs and mitotic cells Student's t-test as the variance was equal and the data were normally distributed. Illustrations of the quantifications are displayed as violin plot,dot plot, bar and pie chart. Each experiment was performed in at least 3 biological replicates.

Result

Cytokinetic bridges (CBs) are present in iEGL

To assess the presence of mitotic cells and CBs in the EGL (as defined by DAPI staining; Figure 1A) in P7 mice, we labeled mitotic cells with an anti-Ki67 antibody and CBs with an anti-Aurora B kinase antibody. Expression of the Transient Axonal Glycoprotein TAG-1 was used to distinguish the iEGL from the oEGL. Mitotic cells displayed a distinct and strong Ki67 expression pattern (Sobecki et al., 2016; Sun & Kaufman, 2018) which we found in high density in the oEGL (**Fig. 1A**) but sparsely in the iEGL (**Fig. 1A** and **Fig. 1B, white arrowhead)**, indicating that some GCs continue to divide within the iEGL. This was further confirmed by anti-Aurora B kinase labelling, indicating the presence of CBs which form at the end of mitosis (**Fig. 1B, yellow arrowhead**). As expected, their proportion in the iEGL was much lower compared to the oEGL which constitutes the primary proliferative zone (**Fig. 1C**). These findings align with previous studies characterizing the EGL as a dynamic proliferative compartment (Cordero Cervantes et al., 2023; Hanzel et al., 2019). Moreover, our quantification of mitotic cells is consistent with our previous finding, despite different methodological approaches (Cordero Cervantes et al., 2023).

To determine whether the previously identified ICs (Cordero Cervantes et al., 2023) correspond exclusively to CBs, we replicated the analysis by comparing the percentage of mitotic cells (prophase, prometaphase, metaphase, anaphase, telophase) with the percentage of CBs in the iEGL (**Fig. 1D**). We found no statistically significant difference between the percentage of mitotic cells (0.69%) and CBs (0.66%). However, the observed frequency of CBs was lower than the frequency of ICs reported in our previous study (3,76%; Cordero Cervantes et al., 2023) suggesting that the iEGL may contain additional types of connection, such as IBs or TNT-like connections.

<u>The EGL appears devoided of IBs</u>

To assess whether IBs are present in the iEGL at P7, we performed quantitative immunofluorescence and analyzed the proliferative states of GCs connected by Aurora B kinase^{+} bridges based on their Ki67 expression patterns and levels. We categorized these connected GCs into three groups: (1) “High Ki67” GCs characterized by strong expression and compact nuclear Ki67 labelling which correspond to cells undergoing mitosis,; (2) “Low Ki67” GCs characterized by low expression and dotted or diffuse Ki67 patterns which correspond to cells in earlier cell cycle phases or that recently exited proliferation, and (3) “No Ki67” GCs showing no Ki67 expression which correspond to cells in late G0, (**Fig. 2A**). We found that

connected GCs were either “High Ki67” (50.75%) or “Low Ki67” (49.25%) GCs (**Fig. 2B),** and we did not observe any Aurora B kinase-positive bridges between “No Ki67” GCs (**Fig. 2A, yellow arrowhead, and 2B).** This suggests that bridges formed during cytokinesis do not persist in quiescent cells, as Ki67 disappears completely within 1-2 days after entering the G0 phase (Miller et al., 2018; Sobecki et al., 2016).

Aurora B kinase has been extensively used as a marker for CBs, however its expression in IBs remains uncharacterized. To further differentiate stable IBs from CBs, we labeled midbody-containing bridges using an anti-citron kinase antibody, which marks midbodies in CBs but not mature IBs (Price et al., 2023) and an anti-anillin antibody, previously reported to label IBs in the Drosophila larval brain (Haglund et al., 2011), (**Fig. 2C**). We found that 81.33% of the bridges were labelled with both Aurora B kinase and anillin (**Fig. 2c$_1$ and 2D**), 2.78% were only labelled with Aurora B kinase (**Fig. 2c$_2$ and 2D**), and 15.89% were only labelled with anillin (**Fig. 2c$_3$ and 2D**). The absence of anillin or Aurora B kinase in those two groups may reflect differences in the timing or levels of protein expression, potentially making them undetectable at certain stages of cytokinesis (Halcrow et al., 2022; Renshaw et al., 2014). Importantly, all 3 groups express the midbody protein citron kinase suggesting that all those ICs are CBs, (**Fig. 2c$_1$-c$_3$ and 2D**). While we cannot fully exclude the presence of IBs due to the lack of well-characterized markers in somatic cells, our data do not support the presence of IBs in the EGL. Thus, these findings suggest that the previously identified ICs (Cordero Cervantes et al., 2023) are not IB and therefore more likely of a different nature.

<u>TNT-like connections are present in the developing cerebellum</u>

To explore the nature of those ICs and test whether they are TNT-like connections, we developed an approach to visualize fine structures between sparsely labelled GCs. Since EGL is densely packed, this should allow us to observe TNTs as they are thin membranous structures characterized by their ability to form between distinct cells. To this end, P5 pups were electroporated at the EGL level with a *pCAG-Dendra2-E2A-GFP-Cep55* plasmid, which sparsely labeled the cytosol of GCs and ICs, and sacrificed at P7. This genetic construct was originally designed to express two separate proteins: Dendra2, marking the cytoplasm of electroporated GCs, and GFP-Cep55, intended to label ICs originating from cell division (CBs/IBs) (Korenkova et al., 2024).

To validate plasmid expression, brain slices were immunostained with anti-GFP and anti-anillin antibodies. We chose anti-anillin over anti-Aurora B kinase to label CBs, as it identified a greater number of CBs (**Fig. 2D**). Anti-citron kinase and anti-Cep55 antibodies were not used due to their punctuated staining patterns, which can create confusion between specific labelling and background. DNA sequence cloning in our vector resulted in a Dendra2-EGFP-Cep55 fusion (**Fig S2**). Consequently, GFP labelling did not specifically label midbodies but instead showed cytoplasmic expression, overlapping with the endogenous Dendra. Thus, to distinguish CBs from TNT-like connections we systematically stained slices with anti-anillin (to label CBs) and anti-GFP (to enhance the endogenous fluorescence present in the cytoplasm of cells) (**Fig. 3A-3C**). We found that 77% of connected pairs did not express Anillin (**Fig. 3D**), suggesting that most ICs were TNT-like connections. This proportion is similar to that reported in gastrula zebrafish embryo, where TNT-like connections, which were also compared to CBs, comprised 81% of ICs (Korenkova et al., 2024). However, unlike zebrafish —where a significant proportion of TNT-like connections were more than 5 µm in length, which allowed them to set length criteria to distinguish CBs/IBs from TNT-like connections—we observed only a modest size difference. Although some TNT-like connections extended beyond 5 µm, their mean length was 5.38 µm, compared to 2.92 µm for CBs (**Fig. 3E**), indicating that connection type could not be reliably distinguished by length alone. To directly observe their formation, we performed time-lapse imaging on acute brain slices, capturing a TNT-like connection developing via a filopodia-driven mechanism, similar to previously described *in vitro* (Korenkova et al., 2020) (**Fig. 3F-3F'**). We observed protrusions extending from each cell (white arrowheads), with the TNT-like structure fully forming within 20 minutes and persisting for at least 10 minutes. Of note, given the lack of evidence for cargo transfer, we cannot rule out the possibility that some of the observed ICs correspond to cytonemes (Korenkova et al., 2020). Since all ICs previously identified with ssSEM were open at both ends (Cordero Cervantes et al., 2023) we speculate that the ICs described here may also be open-ended.

<u>Characteristics of in situ TNT-like connections in the EGL</u>

To complement the experimental description of those connections and determine whether they occur between clonally or non-clonally related GC, we used a Brainbow-derived strategy. Newborn *Nestin-Cre*$^{ERT2+/-}$*; Cytbow*$^{+/+}$ mice received daily subcutaneous tamoxifen injections from P0 to P3 (**Fig4A**; see Methods). Pups were sacrificed at P7 (**Fig. 4A**). Cre-mediated

recombination of the CAG-driven *Cytbow* transgene (Loulier et al., 2014) results in stochastic expression of one of three distinct cytoplasmic fluorescent proteins (mTurquoise2, eYFP, or tdTomato), or a combination of two, in GCs cytoplasm, due to the used of homozygous *Cytbow*$^{+/+}$ animals (**Fig. S3A**). Importantly these fluorescent labels are stably inherited through cell division, enabling us to infer clonal relationships among GCs based on their color. Hence, cells labeled with the same color were considered as clonally related. Reversely, cells labeled with two different colors were considered as non-clonally related, since they cannot originate from the same cell division (**Fig 4A)**. Similar to the *pCAG-Dendra2-E2A-EGFP-Cep55* plasmid electroporation approach, this strategy enabled sparse labeling of GCs, facilitating the identification of connections in the densely populated EGL, particularly in lobule 10 (**Fig. S3B**). Furthermore, connections between clonally related cells should correspond to either CBs or TNT-like connections, while connections between non-clonally related cells (in most cases labeled with different colors) should correspond to TNT-like connections, since they cannot result from cell division. Endogenous fluorescence signals were amplified to optimize optical visualization of these thin structures (**Fig. S3C-E**): the tdTomato signal was enhanced using an anti-tdTomato antibody, and mEYFP was amplified using an anti-GFP antibody which also detected mTurquoise2, and to a certain extent eBFP2 (**Fig. S3C-D**). Importantly, due to the design of the *Cytbow* construct and the sparse labelling, we estimated the probability of a mTurquoise2^{+} GC being connected to an eYFP^{+} GC as very low. This reduces the likelihood of overlooking connections between non-clonally related GCs expressing reporters detected by the anti-GFP antibody. In addition, cerebellar slices were also labelled with an anti-anillin antibody (**Fig. 4A)** to detect CBs between labeled GCs (**Fig. S3E**). We identified both clonally related (87%) (**Fig. 4B, 4D, 4H, S3D**) and non-clonally related (13%) (**Fig. 4C, 4D**) GCs connected via TNT-like connections. Overall, 8.85% of labelled GCs were connected via TNT-like connections (**Fig. 4E)**, a lower proportion than in zebrafish embryos (35%) (Korenkova et al., 2024). This difference may stem from the fact that we are examining two different tissues from two different species, at different developmental stages. It could also result from fixation artifacts, as paraformaldehyde (PFA), immunostaining, and long-light exposures are known to disrupt TNTs, while the data from zebrafish embryos were acquired from live samples without any fixation procedure (Cordero Cervantes & Zurzolo, 2021; Delage et al., 2016; Matejka et al., 2024).

While 79% of connected cells had a single TNT-like connection (**Fig. 4B, F, H**), 21% were connected by multiple connections (**Fig. 4C, F, S3d$_1$**), a feature previously observed *in vitro* (Sáenz-de-Santa-María et al., 2023). Interestingly, these connections could form from soma or neurites like *in vitro* (Tardivel et al., 2016). 54% of these connections formed between GC somas (**Fig. 4b$_1$-b$_2$, 4H, S3d$_1$**), 41% connected a GC soma to another GC's neurite (**Fig. 4c, 4F purple arrowhead**), and 5% connected neurites of two GCs (**Fig. 4F orange arrowhead**). Additionally, based on the DAPI pattern, we observed TNT-like connections connecting dividing (identified by compact chromatin) and non-dividing cells (which displayed more diffuse staining and darker nucleolar regions) (**Fig. 4b$_1$**), a phenomenon previously reported in developing zebrafish (Korenkova et al., 2024). To further assess the mitotic state of connected GCs, cerebellar slices were post-stained with anti-PH3 (mitotic marker Phosphohistone H3) to more reliably identify mitotic cells compared to using DAPI staining alone. Additional staining with anti-anillin was used to exclude CBs, and anti-tdTomato was applied to improve the visualization of TNT-like connections (**Fig. 4H**). We only found TNT-like connections between non-dividing cells, suggesting that connections between dividing and non-dividing cells were very rare (**Fig. 4I**). Indeed, although TNT-like connections were distributed throughout the EGL, their location varied; some were closer to the pia (**Fig. 4b$_1$**), others located in the middle of the EGL (**Fig. 4b$_2$**), but the majority were near the ML border, where GCs are less likely to divide (**Fig. 4C, 4H, S3d$_1$**).

Conclusion

This study identifies ICs in the EGL of the developing mouse cerebellum with a specific focus on CBs, IBs and TNT-like connections. We provide evidence for the presence of CBs in the iEGL and TNT-like connections throughout the EGL, while IBs do not appear to be present in the EGL. The TNT-like connections observed exhibit morphological diversity, appearing as thin or thick projections originating from the soma or neurites, similar to previously described TNTs *in vitro* and *in vivo*. Notably multiple TNT-like connections can form between the same pair of cells, potentially facilitating the transfer of different cellular cargo. Additionally, while granule cells (GCs) predominate in the EGL, our labeling strategy does not exclude the possibility that other cell types contribute to the observed ICs.

Overall, our study aligns with previous findings from connectomic analyses of the mouse cerebellum (Cordero Cervantes et al., 2023), revealing unprecedented connections between

neural cells in the developing brain and excluding a cytokinetic origin for these structures. TNT-like connections may contribute to cerebellar development by enabling long-range, targeted communication before synapse formation. They could coordinate GC migration, akin to the role of TNT-like structures in neural crest cell migration (Teddy & Kulesa, 2004), or influence migration, cerebellar organization, and synaptic development (Kim et al., 2023). Future studies incorporating functional analysis and live-cell imaging will be critical in elucidating the precise roles of these connections in cerebellar circuit formation.

Limitation of the study

While we carefully identified ICs based on 3D morphology, this study could not assess their functional properties. As in all tissue studies, functional validation will be essential to confirm whether these structures are true TNTs enabling molecular exchange or instead represent cytonemes or simple membrane protrusions in close apposition to neighbouring cells. Functional analysis of TNTs, including live imaging to track their dynamics and cargo transfer, as well as genetic or pharmacological disruption of their formation, will be critical to establish their role in cerebellar circuit assembly. While such approaches have been applied in zebrafish embryos (Korenkova et al., 2024), and in interpericyte-TNTs (Alarcon-Martinez et al., 2020), they have not been carried out in the context of cerebellar development. The lack of specific molecular markers for TNTs in neural tissues also limits our ability to distinguish them from other ICs. Addressing these challenges will be essential to fully understand the contribution of TNT-mediated communication to normal cerebellar development and its potential relevance in neurodevelopmental disorders or cerebellar malformations. Ultimately, overcoming these limitations will be key to determining whether TNTs represent a fundamental mechanism of neural circuit formation.

Acknowledgments

The authors would like to acknowledge the help of the following Institut Pasteur facilities: HistoPathology Core Facility, Photonic Bioimaging platform and the Image Analysis Hub. The authors would like to thank Frédéric Doussau for his guidance in performing postnatal electroporation; all members of the Zurzolo group for fruitful discussions, with special thanks to Thea Chrysostomou for helping to implement postnatal electroporation at Institut Pasteur and Olga Korenkova for her technical and scientific feedback.

This work was supported by a dedicated grant called Big Brain Theory Program co-funded by Institut Pasteur and Paris Brain Institute to CZ and LC, the Inception program (Investissement d'Avenir grant) ANR-16-CONV-0005, and Equipe FRM - EQU202103012630 ANR AAPG2023 UnProSec 2024-2027, FRM "MND202310017892" 2023-2027 to CZ, Conseil régional d'Ile-de-France, DIM ELICIT and "Financement de Fin de thèse" de la FRM to GK.

Author contributions

Conceptualization: MR, CZ and LC. Methodology: MR, SL, GK, CZ, LC and JL. Investigation: MR, GK, GV, NDM. Formal analysis: MR, GV. Writing—original draft: MR. writing—review and editing: MR, GV, SL, CZ, LC, GK, JL. Funding acquisition: CZ, LC

Declaration of interests

The authors declare no competing interests.

References

Alarcon-Martinez, L., Villafranca-Baughman, D., Quintero, H., Kacerovsky, J. B., Dotigny, F., Murai, K. K.,...Di Polo, A. (2020). Interpericyte tunnelling nanotubes regulate neurovascular coupling. *Nature*, *585*(7823), 91-95. https://doi.org/10.1038/s41586-020-2589-x

Bahram Sangani, N., Gomes, A. R., Curfs, L. M. G., & Reutelingsperger, C. P. (2021). The role of Extracellular Vesicles during CNS development. *Prog Neurobiol*, *205*, 102124. https://doi.org/10.1016/j.pneurobio.2021.102124

Berger, D. R., Seung, H. S., & Lichtman, J. W. (2018). VAST (Volume Annotation and Segmentation Tool): Efficient Manual and Semi-Automatic Labeling of Large 3D Image Stacks. *Front Neural Circuits*, *12*, 88. https://doi.org/10.3389/fncir.2018.00088

Consalez, G. G., Goldowitz, D., Casoni, F., & Hawkes, R. (2020). Origins, Development, and Compartmentation of the Granule Cells of the Cerebellum. *Front Neural Circuits*, *14*, 611841. https://doi.org/10.3389/fncir.2020.611841

Cordero Cervantes, D., Khare, H., Wilson, A. M., Mendoza, N. D., Coulon-Mahdi, O., Lichtman, J. W., & Zurzolo, C. (2023). 3D reconstruction of the cerebellar germinal layer reveals tunneling connections between developing granule cells. *Sci Adv*, *9*(14), eadf3471. https://doi.org/10.1126/sciadv.adf3471

Cordero Cervantes, D., & Zurzolo, C. (2021). Peering into tunneling nanotubes-The path forward. *EMBO J*, *40*(8), e105789. https://doi.org/10.15252/embj.2020105789

Delage, E., Cervantes, D. C., Pénard, E., Schmitt, C., Syan, S., Disanza, A.,...Zurzolo, C. (2016). Differential identity of Filopodia and Tunneling Nanotubes revealed by the opposite functions of actin regulatory complexes. *Sci Rep*, *6*, 39632. https://doi.org/10.1038/srep39632

Haglund, K., Nezis, I. P., & Stenmark, H. (2011). Structure and functions of stable intercellular bridges formed by incomplete cytokinesis during development. *Commun Integr Biol*, *4*(1), 1-9. https://doi.org/10.4161/cib.4.1.13550

Halcrow, E. F. J., Mazza, R., Diversi, A., Enright, A., & D'Avino, P. P. (2022). Midbody Proteins Display Distinct Dynamics during Cytokinesis. *Cells*, *11*(21). https://doi.org/10.3390/cells11213337

Hall, E. T., Dillard, M. E., Cleverdon, E. R., Zhang, Y., Daly, C. A., Ansari, S. S.,...Ogden, S. K. (2024). Cytoneme signaling provides essential contributions to mammalian tissue patterning. *Cell*, *187*(2), 276-293.e223. https://doi.org/10.1016/j.cell.2023.12.003

Hanzel, M., Rook, V., & Wingate, R. J. T. (2019). Mitotic granule cell precursors undergo highly dynamic morphological transitions throughout the external germinal layer of the chick cerebellum. *Sci Rep*, *9*(1), 15218. https://doi.org/10.1038/s41598-019-51532-y

Kim, M., Jun, S., Park, H., Tanaka-Yamamoto, K., & Yamamoto, Y. (2023). Regulation of cerebellar network development by granule cells and their molecules. *Front Mol Neurosci*, *16*, 1236015. https://doi.org/10.3389/fnmol.2023.1236015

Korenkova, O., Liu, S., Prlesi, I., Pepe, A., Albadri, S., Del Bene, F., & Zurzolo, C. (2024). Tunneling nanotubes enable intercellular transfer in zebrafish embryos. *Dev Cell*. https://doi.org/10.1016/j.devcel.2024.10.016

Korenkova, O., Pepe, A., & Zurzolo, C. (2020). Fine intercellular connections in development: TNTs, cytonemes, or intercellular bridges? *Cell Stress*, *4*(2), 30-43. https://doi.org/10.15698/cst2020.02.212

Lagace , D. C., Whitman, M. C., Noonan, M. A., Ables, J. L., DeCarolis, N. A., Arguello, A. A.,...Eisch, A. J. (2007). Dynamic Contribution of Nestin-Expressing Stem Cells to Adult Neurogenesis. *Journal of Neuroscience*, *27*(46), 12623-12629. https://doi.org/10.1523/JNEUROSCI.3812-07.2007

Loulier, K., Barry, R., Mahou, P., Le Franc, Y., Supatto, W., Matho, K. S.,...Livet, J. (2014). Multiplex cell and lineage tracking with combinatorial labels. *Neuron*, *81*(3), 505-520. https://doi.org/10.1016/j.neuron.2013.12.016

Matejka, N., Amarlou, A., Neubauer, J., Rudigkeit, S., & Reindl, J. (2024). High-Resolution Microscopic Characterization of Tunneling Nanotubes in Living U87 MG and LN229 Glioblastoma Cells. *Cells*, *13*(5). https://doi.org/10.3390/cells13050464

Miller, I., Min, M., Yang, C., Tian, C., Gookin, S., Carter, D., & Spencer, S. L. (2018). Ki67 is a Graded Rather than a Binary Marker of Proliferation versus Quiescence. *Cell Rep*, *24*(5), 1105-1112.e1105. https://doi.org/10.1016/j.celrep.2018.06.110

Palese, F., Rakotobe, M., & Zurzolo, C. (2025). Transforming the concept of connectivity: unveiling tunneling nanotube biology, and their roles in brain development and neurodegeneration. *Physiol Rev*. https://doi.org/10.1152/physrev.00023.2024

Pereda, A. E. (2014). Electrical synapses and their functional interactions with chemical synapses. *Nat Rev Neurosci*, *15*(4), 250-263. https://doi.org/10.1038/nrn3708

Price, K. L., Tharakan, D. M., & Cooley, L. (2023). Evolutionarily conserved midbody remodeling precedes ring canal formation during gametogenesis. *Dev Cell*, *58*(6), 474-488.e475. https://doi.org/10.1016/j.devcel.2023.02.008

Qu, X., Kumar, A., & Bartolini, F. (2021). Live imaging of microtubule dynamics at excitatory presynaptic boutons in primary hippocampal neurons and acute hippocampal slices. *STAR Protoc*, *2*(1), 100342. https://doi.org/10.1016/j.xpro.2021.100342

Renshaw, M. J., Liu, J., Lavoie, B. D., & Wilde, A. (2014). Anillin-dependent organization of septin filaments promotes intercellular bridge elongation and Chmp4B targeting to the abscission site. *Open Biol*, *4*(1), 130190. https://doi.org/10.1098/rsob.130190

Rujano, M. A., Briand, D., Đelić, B., Marc, J., & Spéder, P. (2022). An interplay between cellular growth and atypical fusion defines morphogenesis of a modular glial niche in Drosophila. *Nat Commun*, *13*(1), 4999. https://doi.org/10.1038/s41467-022-32685-3

Sahay, A., Kale, A., & Joshi, S. (2020). Role of neurotrophins in pregnancy and offspring brain development. *Neuropeptides*, *83*, 102075. https://doi.org/10.1016/j.npep.2020.102075

Sobecki, M., Mrouj, K., Camasses, A., Parisis, N., Nicolas, E., Llères, D.,...Fisher, D. (2016). The cell proliferation antigen Ki-67 organises heterochromatin. *Elife*, *5*, e13722. https://doi.org/10.7554/eLife.13722

Stringer, C., Wang, T., Michaelos, M., & Pachitariu, M. (2021). Cellpose: a generalist algorithm for cellular segmentation. *Nat Methods*, *18*(1), 100-106. https://doi.org/10.1038/s41592-020-01018-x

Sun, X., & Kaufman, P. D. (2018). Ki-67: more than a proliferation marker. *Chromosoma*, *127*(2), 175-186. https://doi.org/10.1007/s00412-018-0659-8

Sáenz-de-Santa-María, I., Henderson, J. M., Pepe, A., & Zurzolo, C. (2023). Identification and Characterization of Tunneling Nanotubes for Intercellular Trafficking. *Curr Protoc*, *3*(11), e939. https://doi.org/10.1002/cpz1.939

Tardivel, M., Bégard, S., Bousset, L., Dujardin, S., Coens, A., Melki, R.,...Colin, M. (2016). Tunneling nanotube (TNT)-mediated neuron-to neuron transfer of pathological Tau protein assemblies. *Acta Neuropathol Commun*, *4*(1), 117. https://doi.org/10.1186/s40478-016-0386-4

Teddy, J. M., & Kulesa, P. M. (2004). In vivo evidence for short- and long-range cell communication in cranial neural crest cells. *Development*, *131*(24), 6141-6151. https://doi.org/10.1242/dev.01534

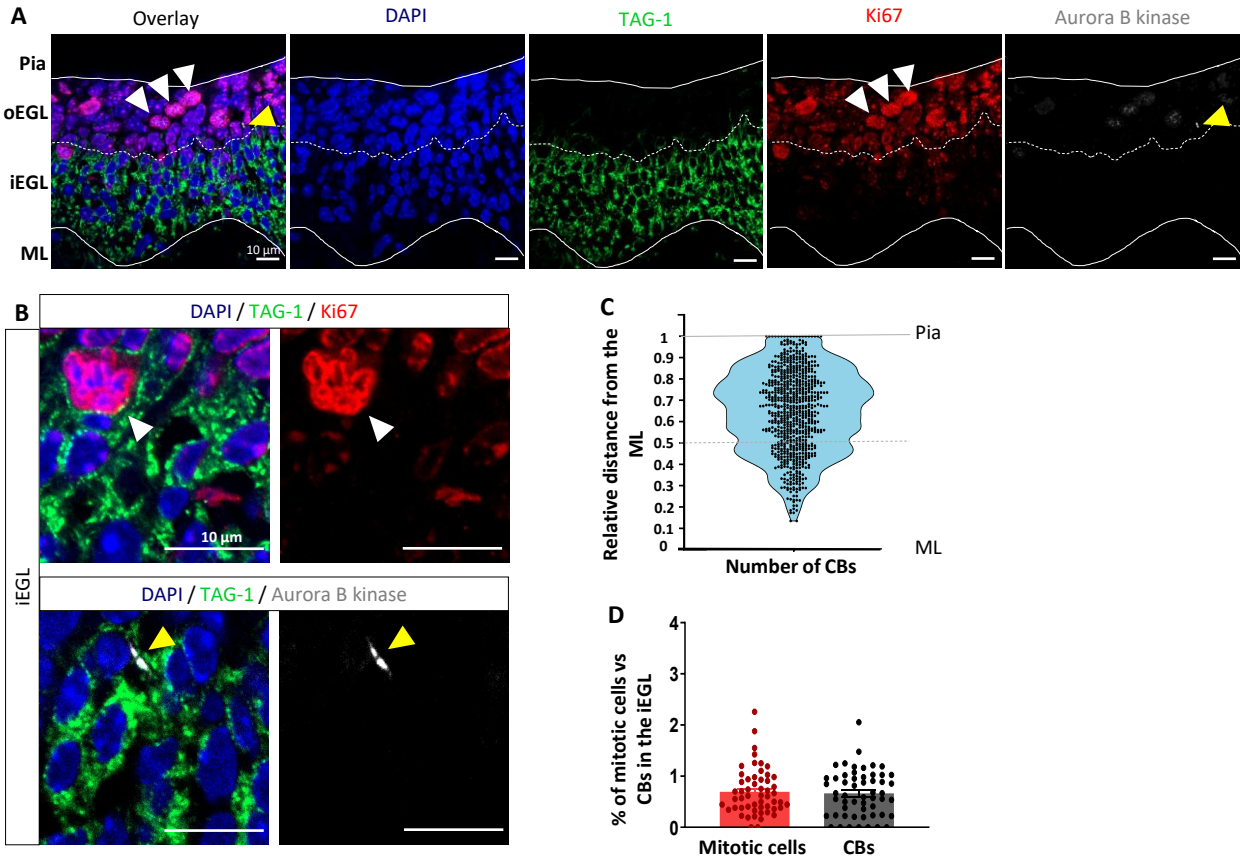

Fig. 1. Assessment of the presence of CBs in the iEGL

(A) Sagittal sections of WT P7 cerebellum labelled with anti-TAG-1 (green), anti-Ki67 (red), anti-Aurora B kinase (grey) and DAPI staining (blue). TAG-1 expression was used to distinguish the iEGL from the oEGL; their border is indicated by the dotted line. Solid lines delineate the EGL, with the pia located above and the ML below. Yellow arrowhead points at a CB and white arrowheads at mitotic cells in the oEGL. (B) Higher magnification showing a mitotic cell (white arrowheads) and CB (yellow arrowhead) in the iEGL. (C) Distribution of CBs throughout the EGL, represented as the relative distance from the ML to the pia. (D) Graph comparing the percentage of mitotic cells (0.69%) and CBs (0.66%) in the iEGL. The data are presented as mean ± SEM; p-value= 0,7 analyzed using a Student t-test. (C-D) N=4 mice, 55 images were analyzed in total. All images correspond to single z-slices and were acquired at x63 magnification.

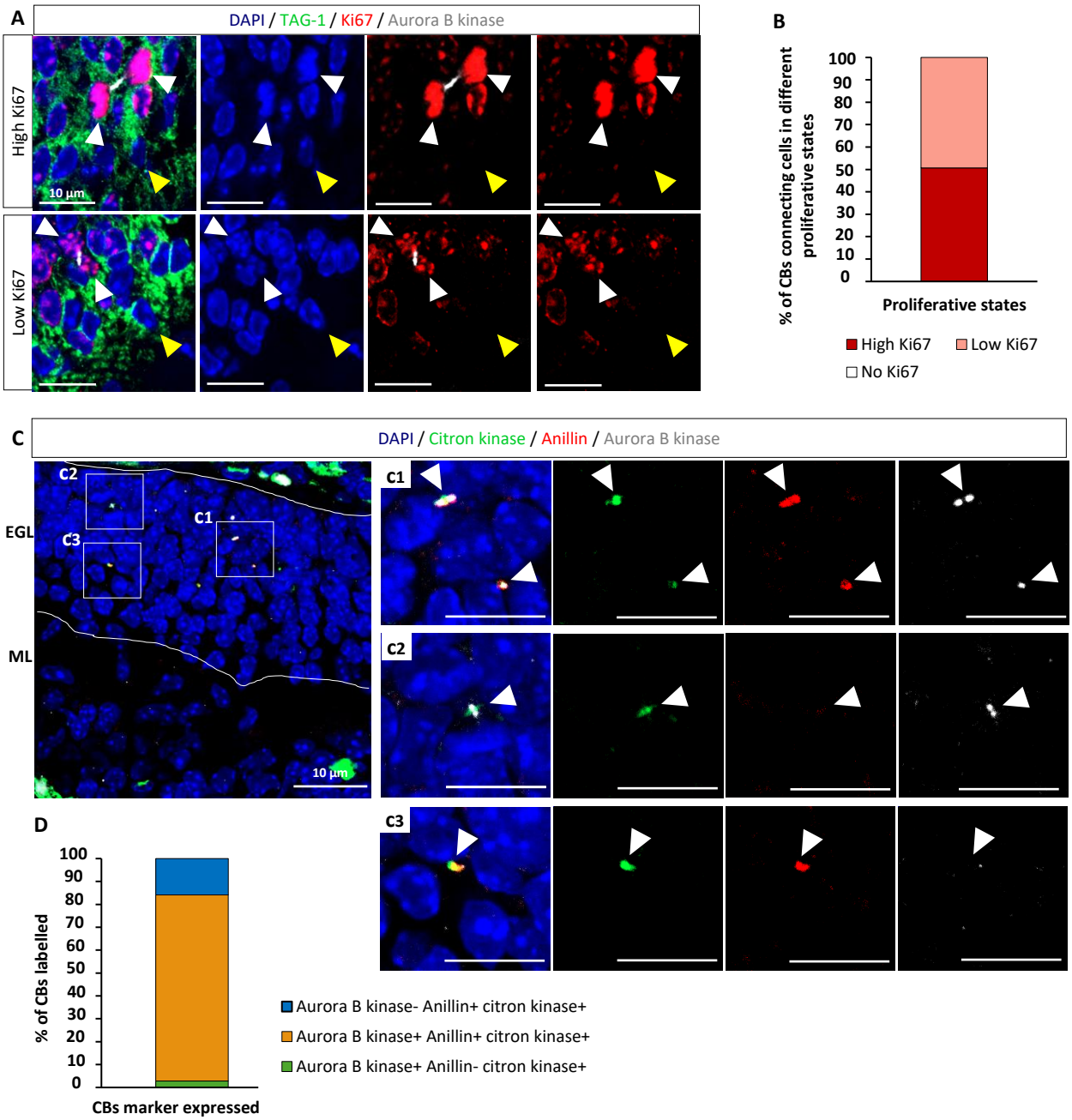
A
DAPI / TAG-1 / Ki67 / Aurora B kinase
High Ki67
Low Ki67
10 µm
B
% of CBs connecting cells in different proliferative states
100
90
80
70
60
50
40
30
20
10
0
Proliferative states
High Ki67
Low Ki67
No Ki67
C
DAPI / Citron kinase / Anillin / Aurora B kinase
EGL
ML
C1
C2
C3
10 µm
D
% of CBs labelled
CBs marker expressed
Aurora B kinase- Anillin+ citron kinase+
Aurora B kinase+ Anillin+ citron kinase+
Aurora B kinase+ Anillin- citron kinase+

Fig. 2. Assessment of the nature of CBs in the iEGL

(A) Sagittal sections of WT P7 cerebellum labelled with anti-TAG-1 (green), anti-Ki67 (red), anti-Aurora B kinase (grey) and DAPI staining (blue). The expression of TAG-1 was used to identify the iEGL. Solid lines delineate the EGL. The white arrowheads show Ki67+ cells that are connected by a CB. The yellow arrowheads show Ki67- cells, which were never observed to be connected by a CB. (B) Repartition of CBs connecting cells in the different proliferative states in the iEGL. The proliferative state is determined based on the pattern and expression level of Ki67. “High Ki67” (50.74%) represents cells that are undergoing mitosis, “Low Ki67” (49.25%) represents cells in earlier cell cycle phases or those that have recently exited proliferation, “No Ki67” (0%) represents cells in late G0. N=4 mice, 55 images were analyzed in total. (C) Labelling with anti-citron kinase (green), anti-anillin (red), anti-Aurora B kinase (grey) and DAPI staining (blue). (c1-c3) Higher magnification of the areas indicated in (C), showing CBs labelled with both anillin and Aurora B kinase (c1), only Aurora B kinase (c2) or only anillin (c3). All CBs expressed citron kinase. (D) Proportion of CBs in the categories shown in c1-c3: 81.33% were Aurora B kinase+/Anillin+/citron kinase+, 2,78% were Aurora B kinase+/Anillin-/citron kinase+, and 15,89% labelled Aurora B kinase-/Anillin+/citron kinase+. N=4 mice, 66 images were analyzed in total. Pannel (A) corresponds to a z-slice, (C) and (c_1-c_3) are maximum projections of 6 z-slices (z-step=0,35 µm). All images were acquired at x63 magnification.

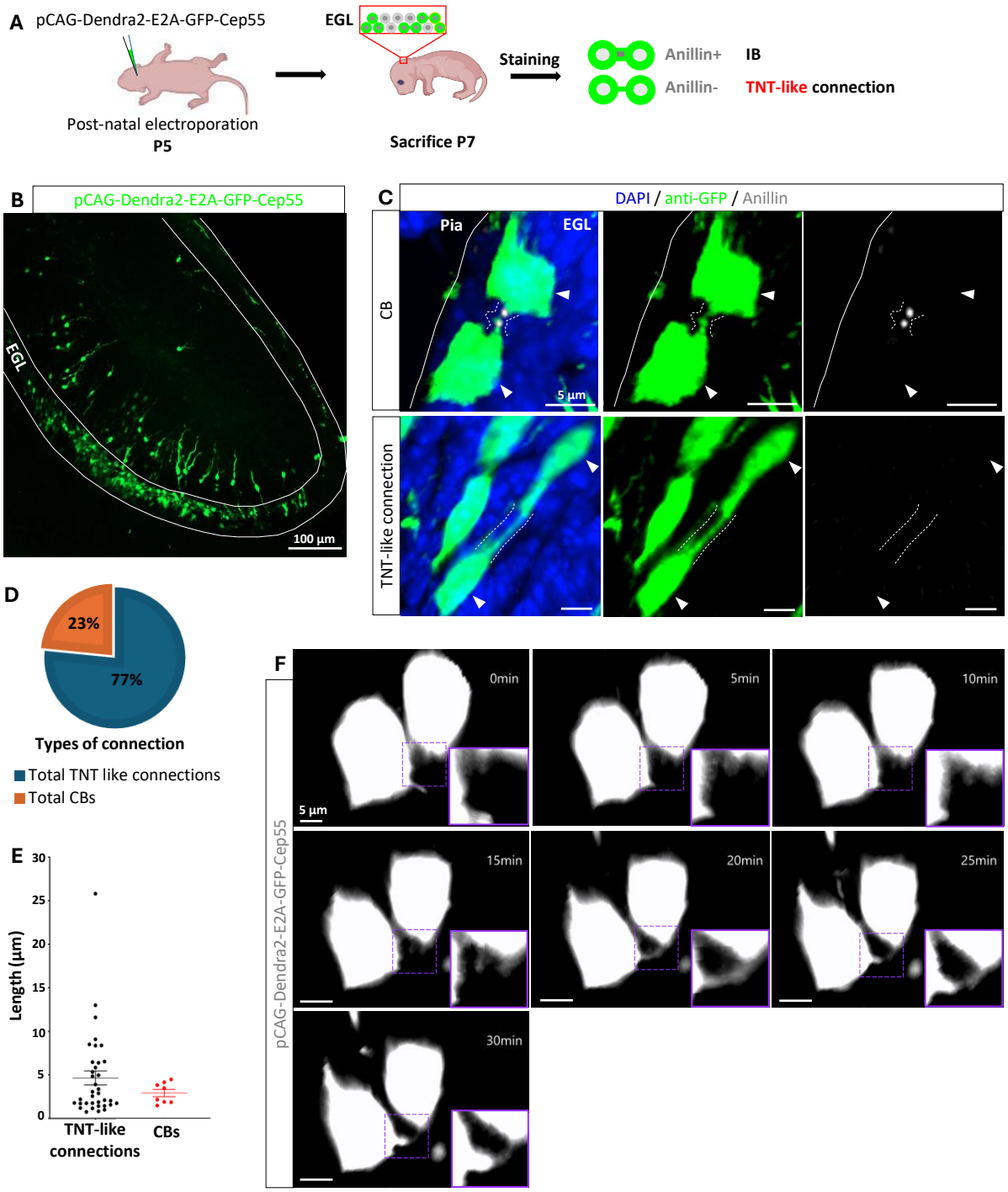
A
pCAG-Dendra2-E2A-GFP-Cep55
Post-natal electroporation
P5
EGL
Sacrifice P7
Staining
Anillin+
IB
Anillin-
TNT-like connection
B
pCAG-Dendra2-E2A-GFP-Cep55
EGL
100 µm
C
DAPI / anti-GFP / Anillin
Pia
EGL
CB
5 µm
TNT-like connection
D
23%
77%
Types of connection
Total TNT like connections
Total CBs
E
Length (µm)
TNT-like connections
CBs
F
pCAG-Dendra2-E2A-GFP-Cep55
0min
5min
10min
15min
20min
25min
30min
5 µm

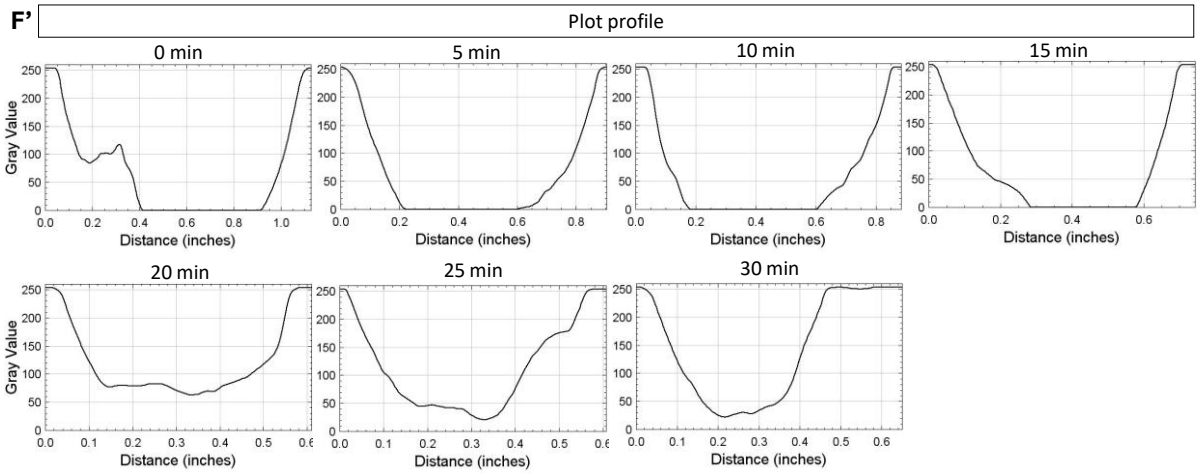
F'
Plot profile
0 min
5 min
10 min
15 min
20 min
25 min
30 min
Gray Value
Distance (inches)

Fig. 3. Identification of TNT-like connections

(A) Schematic representation of the strategy used to sparsely label cells and visualize ICs: The pCAG-Dendra2-E2A-GFP-Cep55 plasmid is electroporated in the EGL of P5 pups. The pups are sacrificed at P7 and cerebellar slices were stained with anti-anillin to distinguish CBs from TNT-like connections. (B) Representative image showing the expression of the plasmid in the EGL. (C) Labelling of sagittal cerebellar slices, at the level of the EGL, with anti-GFP (green), anti-anillin (grey) and DAPI staining showing a CB (anillin+ connection) and a TNT-like connection (anillin- connection). The white arrowheads point at the connected cells. Dotted lines delineate the connections. (D) Graph representing the proportion of CBs and TNT-like connections over the total number of ICs identified. (E) Length of the connections identified in (D) showing an average TNT-like connections and IB's length of 5,38 µm and 2,92 µm, respectively. (D-E) N=3 mice, 36 TNT-like connections and 11 CBs identified, 83 images were analyzed in total. Although cells were labelled, no connections were found in the EGL of one mouse, likely due to the rarity of these connections. In (E) data are presented as mean ± SEM; p-value= 0,09 analyzed using a Welch t-test. (F) Example of TNT-like connection forming between two cells, via the filopodia driven mechanism in a sagittal cerebellar slice. A zoomed-in view of the area where the connection forms (indicated by the dotted purple square) is shown in the bottom right corner of each time point. The two protrusions establish connection approximately 20 min after the start of the recording. (F') Plot profile of the connection shown in (F) at the different time points, showing a continuous connection (grey value > 0) between 20-30 min. Panel (B) shows a z-maximal projection at x10 magnification. (C,F) images correspond to 3D views at x60 magnification. Solid lines delineate the EGL.

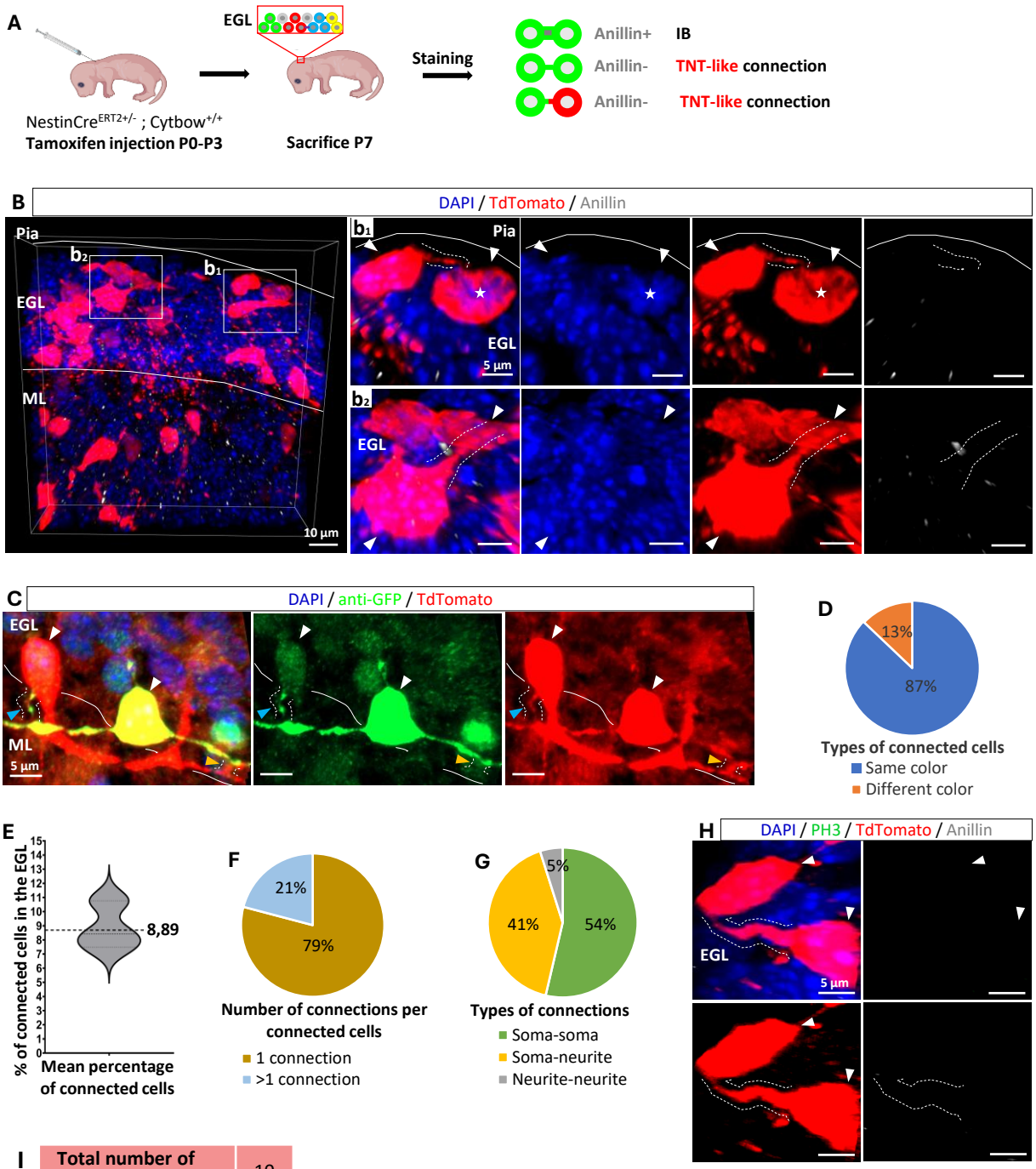

	Total number of connections	10
TdTomato+ cells	% of connections between a pair of PH3- cells	100
	% of connections between a PH3+ and a PH3- cells	0
	% of connections between a pair of PH3+ cells	0

Fig. 4. Assessment of the features of TNT-like connections in the EGL

(A) Schematic representation of the strategy used to sparsely label cells and visualize ICs: *NestinCre*$^{ERT2+/-}$ *; Cytbow*$^{+/+}$ mice were injected with tamoxifen between P0 and P3 to induce the mosaic expression of mTurquoise 2, eYFP, TdTomato or a combination of two of these reporters in neurons. Mice were sacrificed at P7 and were stained with DAPI, anti-anillin (grey) to distinguish CBs from TNT-like connections, anti-GFP (green) and anti-TdTomato (red) to amplify reporter signals and differentiate clonally vs. non-clonally related cells. (B) Representative image of TNT-like connections (anillin-) between TdTomato+ cells in the EGL. (b_1- b_2) Represent a higher magnification of the areas indicated in (B) showing TNT-like connections close to the pia (b_1) and in the middle of the EGL (b_2). The asterisk marks a dividing cell, as identified by the DAPI pattern. (C) Representative image showing a TNT-like connection between a TdTomato+ cell and a TdTomato+GFP+ cell near the ML border. The blue arrowhead points at a connection formed between the soma and neurite. The orange arrowhead points at a connection between the neurites. (D) Graph presenting the percentage of TNT-like connection between same-color vs. different-color cells. (E) Graph representing the relative percentage of connected cells (67 anillin- connections) over the total labelled population (789 labelled cells). The dotted line indicates the mean. SEM is ± 0,061. (F) Graph presenting the percentage of cells forming one vs. multiple (>1) TNT-like connections. (G) Graph presenting the percentage of TNT-like connections categorized by location: soma-soma, neurite-neurite, soma-neurite. (H) Labelling of EGL sagittal sections with anti-PH3 (in green), anti-Tdtomato (in red), anti-anillin (in grey) and DAPI staining (in blue). (J) Spatial distribution of connected (I) Quantification representing the percentage of TNT-like connections (anillin-) between non-dividing cells (PH3-), dividing cells (PH3+), one dividing (PH3+) and one non-dividing cell (PH3-) cells across the EGL. (b_1-b_2, C, F, I) The white arrowheads indicate connected cells. The dashed lines delineate TNT-like connections. (D-E, G-H, K) N=3 mice, 200 images. (I-J) N=3 mice, 86 images. All images correspond to 3D views and were taken at x63 magnification. Solid lines delineate the EGL. Dotted lines delineate the connections.

A.

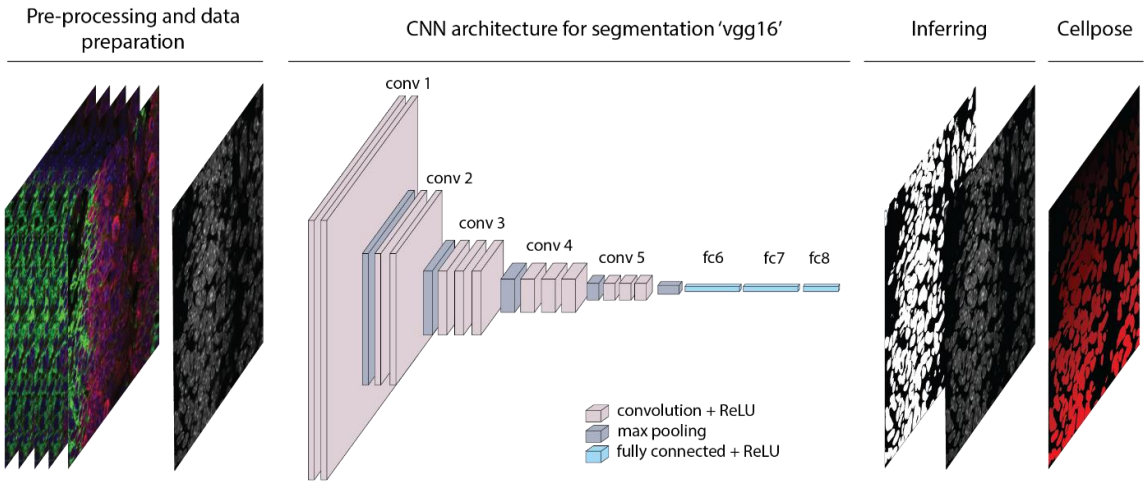
Pre-processing and data preparation
CNN architecture for segmentation 'vgg16'
Inferring
Cellpose
conv 1
conv 2
conv 3
conv 4
conv 5
fc6
fc7
fc8
convolution + ReLU
max pooling
fully connected + ReLU

B.

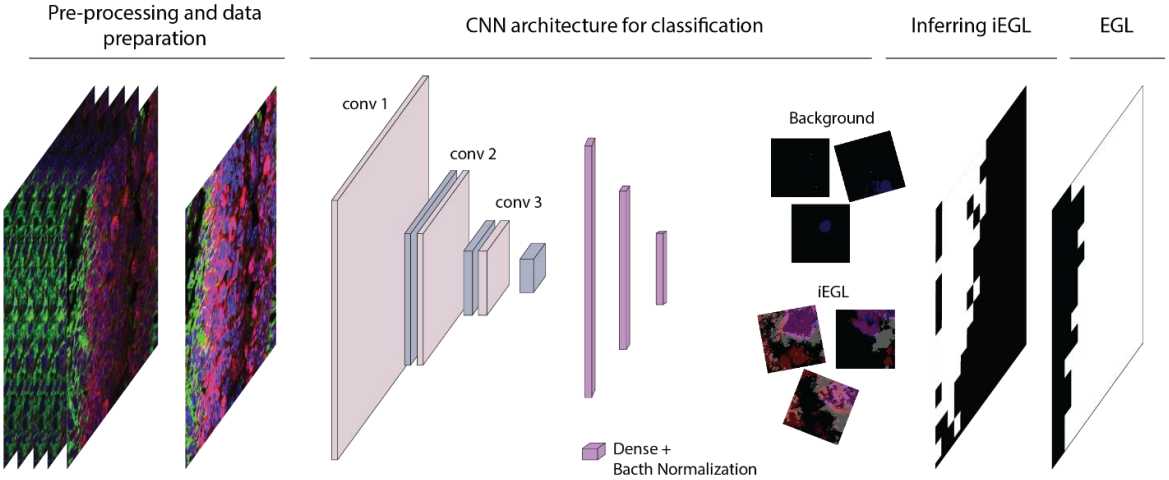
Pre-processing and data preparation
CNN architecture for classification
Inferring iEGL
EGL
conv 1
conv 2
conv 3
Background
iEGL
Dense +
Bacth Normalization

C.

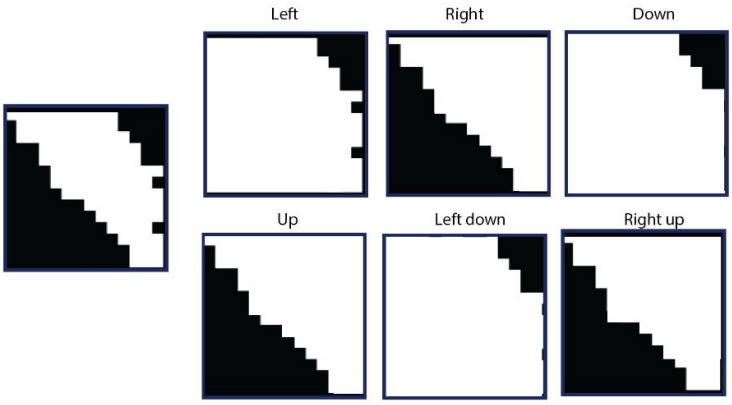
Left
Right
Down
Up
Left down
Right up

D.

D'.

Fig. S1. Image processing in the EGL.

(A) Schematic representation of the steps used for nuclei counting pipeline. The DAPI channel is processed through a CNN-based architecture, followed by nuclei segmentation using the Cellpose software. (B) Schematic showing the delineation of the EGL and iEGL borders for nuclei quantification. DAPI, Ki67 and TAG-1 channels are input to the CNN. The DAPI signal is used to define the EGL while Ki67 and TAG-1 delineate the borders of the iEGL. A classification step distinguishes the iEGL from the rest of the EGL, generating a mask specific to these regions. (C) Illustration of how EGL masks are created based on cerebellum orientation in the image. Orientations include “Left”, “Right”, “Down”, “Up”, ”Left down” or “Right up”. All regions in these orientations are considered part of the iEGL. The images primarily contain the EGL and a small portion of the molecular layer (ML), which contains few nuclei, minimizing quantification errors. (D) Visualization of nuclei identified within the defined masks. Only nuclei located within the mask created - representing either the full EGL or the iEGL - are included in the quantification.

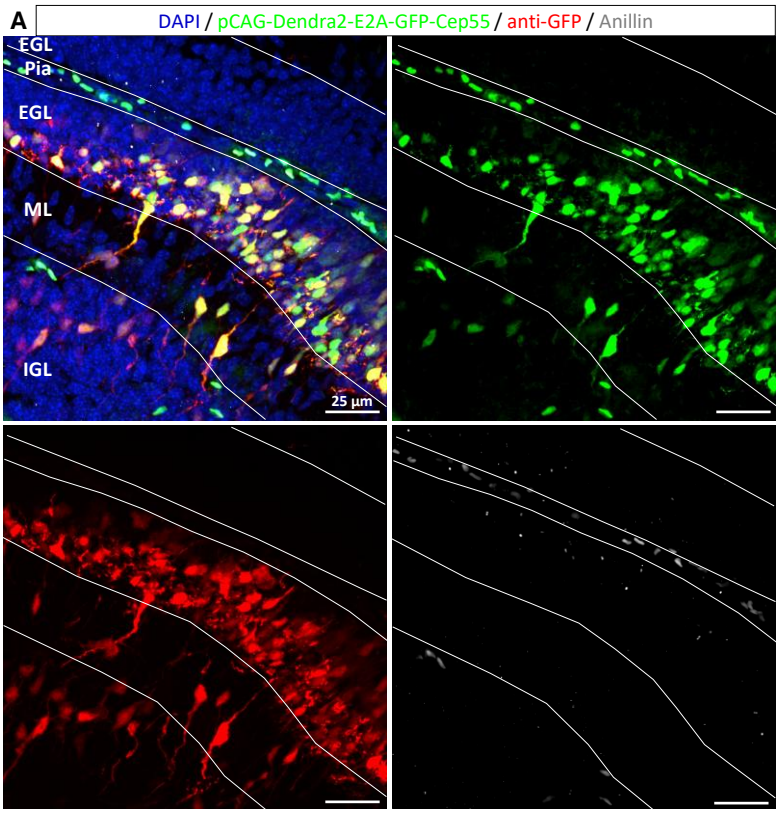

Fig. S2. Validation of the pCAG-Dendra2-E2A-GFP-Cep55 construct

(A) Representative image of P7 sagittal cerebellar sections electroporated with the pCAG-Dendra2-E2A-GFP-Cep55 construct (green). Sections were stained with anti-GFP (red), anti-anillin (grey) and DAPI, showing that the anti-GFP antibody labels the cytoplasm rather than being exclusively localized to the midbody of electroporated cells. All the images correspond to z-maximum projections and were taken at x10 magnification. Solid lines delineate the different layers of the cerebellum

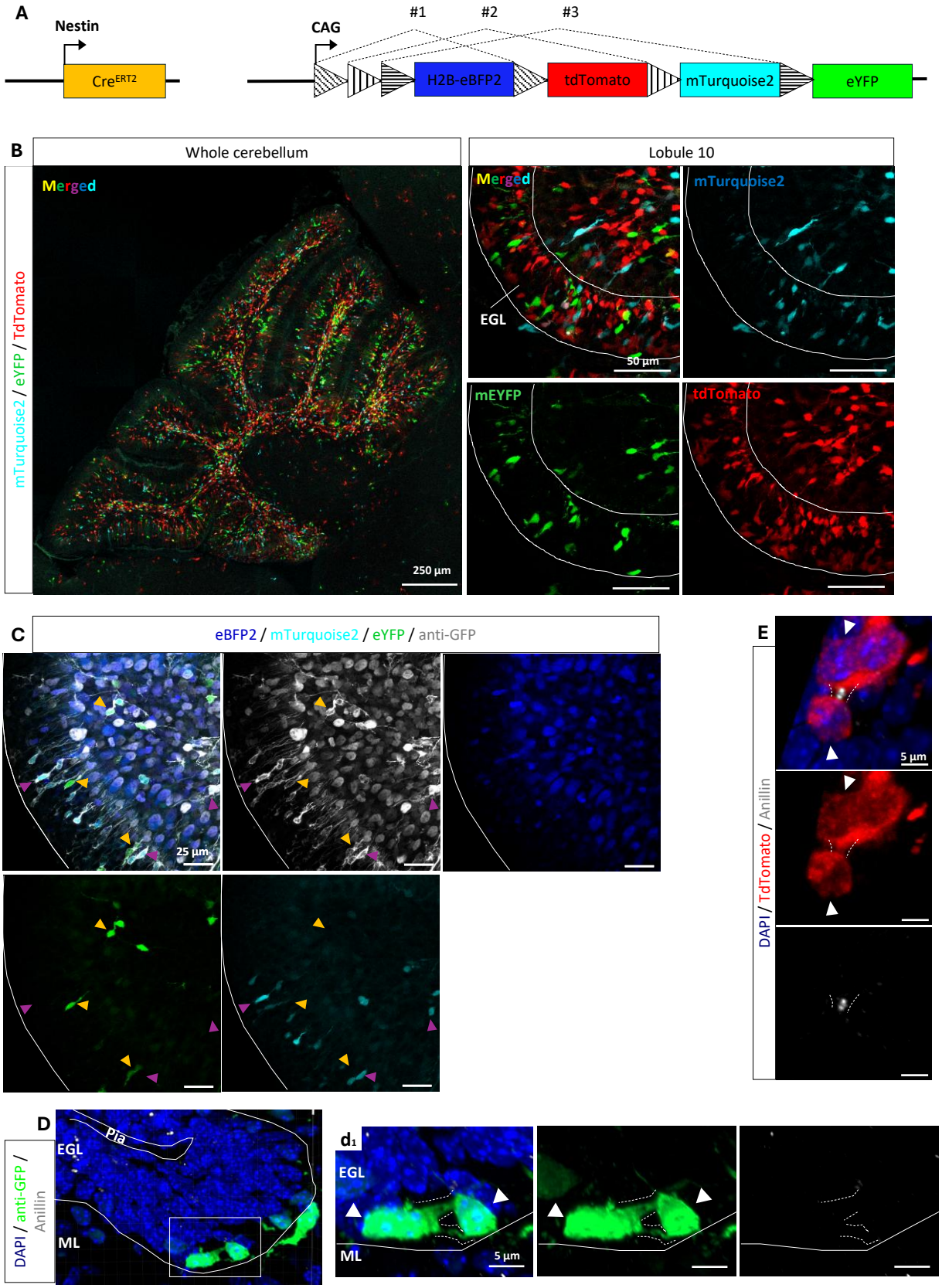
A
Nestin
CreERT2
CAG
#1
#2
#3
H2B-eBFP2
tdTomato
mTurquoise2
eYFP
B
Whole cerebellum
Lobule 10
mTurquoise2 / eYFP / TdTomato
Merged
250 µm
Merged
mTurquoise2
EGL
50 µm
mEYFP
tdTomato
C
eBFP2 / mTurquoise2 / eYFP / anti-GFP
25 µm
E
DAPI / TdTomato / Anillin
5 µm
D
DAPI / anti-GFP / Anillin
Pia
EGL
ML
d1
EGL
ML
5 µm

Fig. S3. Validation of the NestinCre^{ERT2} Cytbow transgenic line

(A) Schematic representation of the *NestinCre$^{ERT2+/-}$; Cytbow$^{+/+}$* transgenic line used to sparsely label cells. This transgenic line expresses nuclear eBFP2 by default. Upon tamoxifen injection, Cre-recombination occurs on the CAG-driven *Cytbow* transgene (Kumamoto et al., 2020). Three mutually exclusive recombination possibilities allow Cre-expressing cells to express a distinct cytoplasmic fluorescent protein: mTurquoise2, mEYFP and TdTomato, in a completely random manner. Since the mice used are homozygous for the *Cytbow* transgene, cells can also express a combination of two reporters. (B) Representative image of P7 sagittal sections showing the endogenous expression of *Cytbow* reporters after tamoxifen injection (P0-P3), in the whole cerebellum, and in the EGL at the level of the lobule 10 where its expression is more pronounced. (C) Labelling with anti-GFP (grey) confirming that it recognizes eBFP2 (blue), mTurquoise2 (Turquoise) and eYFP (green) reporters. Magenta arrowheads highlight mTurquoise2+ cells, while orange arrowheads highlight eYFP+ cells. (D) Labelling with anti-GFP (green), anti-anillin (grey) and DAPI staining (blue), showing that the anti-GFP staining helps identify TNT-like connections (anillin-). (d1) Represents a higher magnification of the area indicated in (D) showing two TNT-like connections (anillin-) between a pair of GFP+ cells at the ML border. The white arrowheads indicate connected cells. Dashed lines delineate TNT-like connections. (E) Labelling of EGL with anti-TdTomato (red), anti-anillin (grey) and DAPI staining (blue). The white arrowheads indicate TdTomato+ cells connected via a CB (anillin+ connection). Dashed lines delineate the CB structure. (B-C) images correspond to z-maximum projections. (C-E) images correspond to 3D views. Images were taken at x20 (B) and x63 (C-E) magnification. Solid lines delineate the EGL. Dotted lines delineate the connections.